















Production, Transport, and Destruction of Dust in the Kuiper Belt: The Effects of Refractory and Volatile Grain Compositions

Thomas Corbett^{1,2} , Alex Doner^{1,2} , Mihály Horányi^{1,2} , Pontus Brandt³ , Will Grundy⁴ , Carey M. Lisse³ , Joel Parker⁵ , Lowell Peltier^{6,7} , Andrew R. Poppe⁸ , Kelsi N. Singer⁵ , S. Alan Stern⁵ , and Anne J. Verbiscer⁹ 

¹Laboratory for Atmospheric and Space Physics, University of Colorado, Boulder, CO, USA; Thomas.Corbett@lasp.colorado.edu

²Department of Physics, University of Colorado, Boulder, CO, USA

³The Johns Hopkins University Applied Physics Laboratory, Laurel, MD, USA

⁴Lowell Observatory, Flagstaff, AZ, USA

⁵Southwest Research Institute, Boulder, CO, USA

⁶National Research Council of Canada, Herzberg Astronomy and Astrophysics Research Centre, Victoria, BC, Canada

⁷Department of Physics and Astronomy, University of Victoria, Victoria, BC, Canada

⁸Space Sciences Laboratory, University of California, Berkeley, CA, USA

⁹Department of Astronomy, University of Virginia, Charlottesville, VA, USA

Received 2024 December 2; revised 2025 January 9; accepted 2025 January 17; published 2025 January 30

Abstract

The Venetia Burney Student Dust Counter (SDC) on board the New Horizons spacecraft measures the spatial and size distributions of dust along its trajectory. Models based on early SDC measurements predicted a peak dust number density at a heliocentric distance of ~ 40 au, followed by a rapid decline. Instead, SDC observed dust fluxes 2–3 times higher than predicted between 40 and 60 au. One potential explanation for this discrepancy is that SDC may be encountering icy grains with different dynamical behavior than previously modeled silicate grains. Due to ultraviolet photosputtering, water–ice grains rapidly erode and migrate outward, significantly contributing to the measured dust number densities only at distances $\gtrsim 40$ au. We present a model of silicate and ice grain dynamics in the outer solar system, considering gravitational and radiation forces and grain erosion. Using SDC data, we estimate that the mass production rate of ice grains between 0.1 and $10 \mu\text{m}$ in the Kuiper Belt (KB) would need to be 20–70 times higher than that of silicate grains. However, KB grains are expected to be refractory/volatile mixtures rather than pure silicate or ice. Thus, we briefly explore simple models of more realistic mixed-grain cases to further gauge the effects of grain composition on the equilibrium dust distribution. Future SDC measurements at greater distances will test the model predictions and further constrain silicate and ice grain production rates in the KB.

Unified Astronomy Thesaurus concepts: [Interplanetary dust \(821\)](#); [Astrophysical dust processes \(99\)](#)

1. Introduction

The Venetia Burney Student Dust Counter (SDC) on board the New Horizons spacecraft is the first dedicated dust instrument to make in situ measurements beyond a heliocentric distance of 18 au. The 0.1 m^2 polyvinylidene fluoride sensor detects changes in surface charge density due to hypervelocity dust impacts (M. Horányi et al. 2008). The measured impact-generated charge is a function of the impactor's mass and velocity (D. James et al. 2010; M. Piquette et al. 2020). Grain mass can be calculated using laboratory calibrations, spacecraft velocity, and the assumption of a circular Keplerian orbit for the impactor. The instrument's electronics have been stable since its launch in 2006 (G. Fountain et al. 2023), and its observations have been periodically reported in the literature (A. Poppe et al. 2010; D. Han et al. 2011; J. R. Szalay et al. 2013; F. Bagenal et al. 2016; M. Piquette et al. 2019; E. Bernardoni et al. 2022; A. Doner et al. 2024).

SDC measurements have been used to estimate the Kuiper Belt (KB) grain production rate and initial ejecta size distribution from the measured spatial and size distributions throughout the solar system (D. Han et al. 2011; A. R. Poppe 2016; A. R. Poppe et al. 2019). Based on SDC data from 5 to

40 au, early models predicted a peak number density of $\sim 30 \text{ km}^{-3}$ for grains above the SDC mass threshold ($m \geq 2.62 \times 10^{-12} \text{ g}$) at a distance of ~ 40 au. The number density was also predicted to decrease by a factor of ~ 2 by 50 au with a continued decline at greater distances (A. R. Poppe 2016; A. R. Poppe et al. 2019). Contrary to expectations, however, SDC reported roughly constant fluxes between 40 and 60 au (A. Doner et al. 2024).

Possible explanations for the higher-than-expected dust fluxes beyond 40 au include radiation pressure extending the grain distribution beyond their source objects, the production of grains with different dynamical behavior than silicate grains, and the expectation of more dust-producing objects than previous models allowed for (A. Doner et al. 2024).

While radiation pressure initially extends the distribution of small grains beyond their source objects, equilibrium distribution is governed by long-term processes, such as Poynting–Robertson (PR) drag (S. P. Wyatt & F. L. Whipple 1950; J. A. Burns et al. 1979). Radiation pressure alone cannot explain the observed higher number densities reported by SDC as it would not cause the originally predicted dust density peak to shift outward beyond 40 au (A. Doner et al. 2024).

Here, we focus on the possibility of a population of grains with different dynamical behavior than silicate grains. Kuiper Belt Objects (KBOs) have surfaces that are a mixture of rocky, carbonaceous, and icy material (M. E. Brown 2012; M. E. Brown & W. C. Fraser 2023), which, in response to

mutual collisions and bombardment, produce rock grains, carbonaceous grains, ice grains, or mixed-composition grains. While previous models assumed only silicate grains, here we consider the test case in which both pure silicate and pure ice grains are produced to gauge the difference in their dynamical behavior. Ice grains undergo rapid destruction by ultraviolet (UV) photospattering and therefore exhibit different dynamical behavior than silicate grains (A. Grigorieva et al. 2007). We also consider that the KB may extend much beyond our current estimates (W. C. Fraser et al. 2024).

2. Grain Dynamics

Newly released grains initially share the dynamical state vector of their source object. Radiation pressure induces an instantaneous potential change, effectively reducing the solar mass by a factor of $1 - \beta$, where β is defined as F_r/F_g , the ratio of the radiation pressure force over gravity from the Sun. The parameter β is a function of the size and density of the grain and remains independent of the heliocentric distance (J. A. Burns et al. 1979).

The subsequent orbital evolution of the grain is governed by PR drag, causing the grain to lose energy and angular momentum over longer timescales (S. P. Wyatt & F. L. Whipple 1950). Gravitational interactions with the giant planets also influence grain dynamics (J.-C. Liou et al. 1999). Without planetary perturbations, the trajectory of a grain is given by the equation of motion

$$\ddot{\mathbf{r}} \approx \frac{\mu}{r^2} \left[(\beta - 1)\hat{\mathbf{r}} - \beta \frac{\mathbf{v}}{c} \right], \quad (1)$$

where \mathbf{r} is the heliocentric position vector of the grain; μ is the standard gravitational parameter of the Sun equal to GM_\odot , with the gravitational constant G and solar mass M_\odot ; \mathbf{v} is the velocity vector of the grain; and c is the speed of light. The $\hat{\mathbf{r}}$ term includes both gravity from the Sun and radiation pressure, while the \mathbf{v} term is the PR drag.

The fastest erosion process for silicate grains is solar-wind-induced sputtering, with a rate of $\sim 0.2 \text{ \AA yr}^{-1}$ at 1 au (T. Mukai et al. 2001). Ice undergoes much more rapid erosion due to UV photospattering, with a rate of $\sim 40 \text{ \AA yr}^{-1}$ at 1 au (H. Harrison & R. I. Schoen 1967; R. W. Carlson 1980). Both rates decrease with heliocentric distance as $1/r^2$. Ice also experiences sublimation, but this process is much slower in the outer solar system than UV photospattering due to the low local equilibrium temperatures (H. Patashnick & G. Rupprecht 1977; C. M. Lisse et al. 2021).

Grains with slow erosion rates, like silicate grains, migrate inward due to PR drag, whereas grains with rapid erosion rates, like ice, initially migrate outward as the continually increasing radiation pressure can overcome PR drag (A. Grigorieva et al. 2007). As the grain continues to erode, its radiation pressure coefficient reaches a maximum and begins to decrease (J. A. Burns et al. 1979). Eventually, the grain begins to migrate inward. This inward migration due to decreasing radiation pressure occurs only for grains below the SDC mass threshold. Figure 1 shows the orbital evolution of example silicate and ice grains.

3. Source Objects

Jupiter-family comets, Halley-type comets, the asteroid belt, and the Trojan asteroids are the dominant source of dust in the

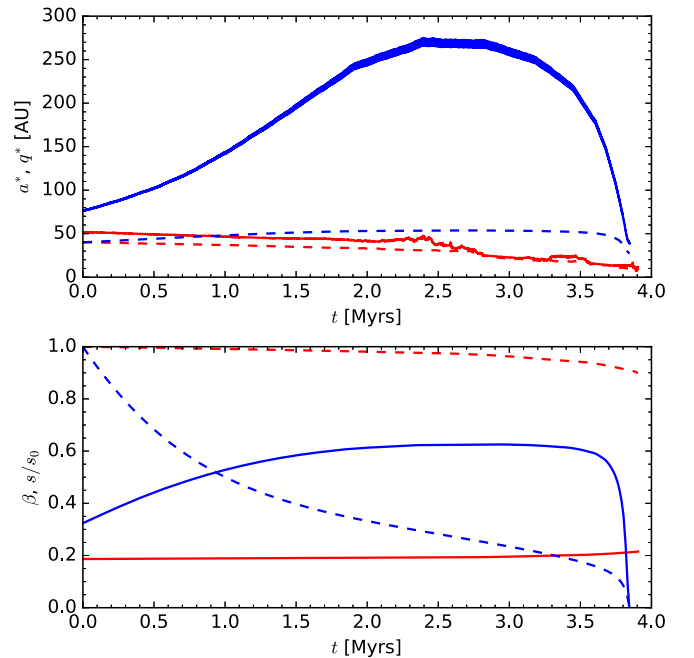


Figure 1. Numerically integrated orbital evolution of initially $1 \mu\text{m}$ radius silicate (red) and ice (blue) grains from a source object on a circular orbit at 40 au, inclined by 5° . Top: evolution of the modified semimajor axis (solid) and modified perihelion distance (dashed). These modified orbital elements are calculated with $\mu^* = \mu(1 - \beta)$ and represent the grain's orbital geometry. Bottom: evolution of radiation pressure parameter (solid) and the ratio of grain size to initial grain size (dashed).

inner solar system, while the KB is the dominant source of dust in the outer solar system (M. Landgraf et al. 2002; A. R. Poppe 2016). Oort cloud comets contribute to the dust density only around 5–10 au and are otherwise negligible (A. R. Poppe 2016). KB dust production mainly results from mutual collisions (S. A. Stern 1996) and interstellar dust bombardment (S. Yamamoto & T. Mukai 1998) at similar rates.

We use various KBO databases/models to investigate the effects of an extended KB. The least extended list of KBOs is NASA/JPL's Small Bodies Database (SBDB), a database of objects with orbital elements determined by direct observation. The Canada-France Ecliptic Plane Survey (CFEPS), which applies a survey simulator to correct for observational biases, includes more distant objects with higher eccentricities and inclinations as well as densely populated mean-motion resonances with Neptune (J. J. Kavelaars et al. 2009; B. Gladman 2010; J. M. Petit et al. 2011). The Outer Solar System Origins Survey (OSSOS) is the most recent and comprehensive debiased KBO model, containing over 26 million modeled objects (M. T. Bannister et al. 2016, 2018; S. M. Lawler et al. 2018). Figure 2 shows the orbital distributions of each KBO database/model, normalized to an area of 1 for comparison.

4. Dust Production

Dust production in the KB can be approximated by ejecting a grain at a random time within the orbit of a randomly selected KBO. This approximation is consistent with ejection via interstellar dust bombardment or other mechanisms independent of heliocentric distance (D. V. Belousov & A. K. Pavlov 2024) but not with mutual collisions, since those will preferentially occur closer to perihelion, where the objects have higher orbital speeds and spatial densities.

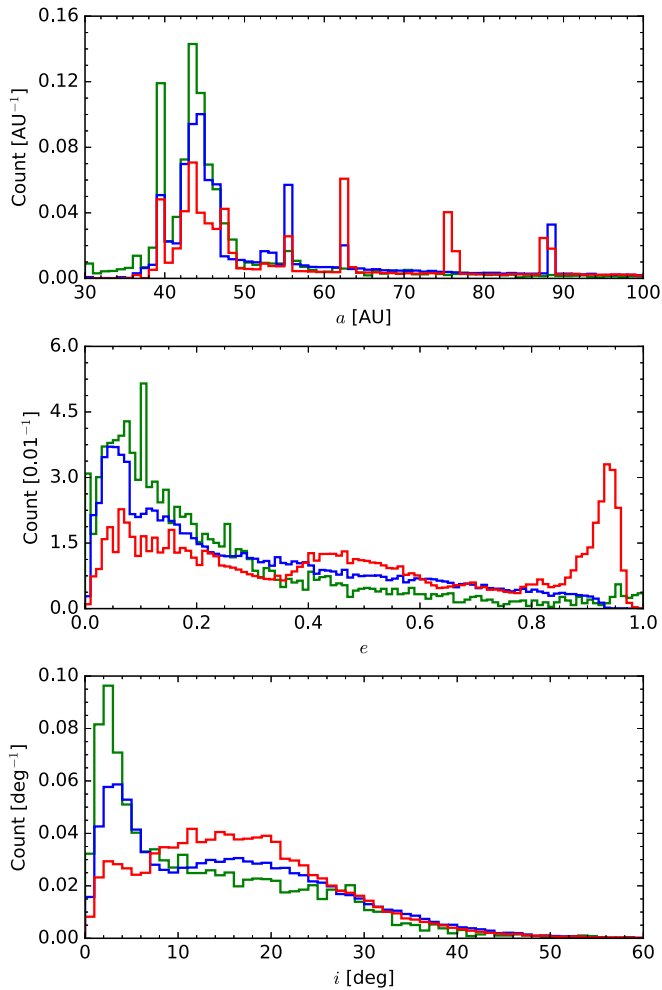


Figure 2. Normalized distributions of KBO orbital elements. From top to bottom: the semimajor axis, eccentricity, and inclination of the SBDB (green), CFEPS (blue), and OSSOS (red) distributions.

The semimajor axis, eccentricity, and inclination of the KBO are obtained from the respective KBO database/model, and the orbital orientation is determined by assigning random values to the longitude of the ascending node ($0 \leq \Omega \leq 2\pi$) and the argument of periapsis ($0 \leq \omega \leq 2\pi$). The ejection position and velocity are calculated by solving Kepler's equation $M = E - e \sin(E)$ (J. M. A. Danby 1992) to determine the eccentric anomaly, E , using a randomly selected mean anomaly ($0 \leq M \leq 2\pi$). The choices of these orbital elements fully determine the initial position \mathbf{r} and velocity \mathbf{v} of a released grain.

Initial grain radius, s , is randomly sampled following a power-law distribution, $n(s) \propto s^{-\alpha}$, with $\alpha = 3.5$, consistent with a collisional equilibrium and observed dust disks (J. S. Dohnanyi 1969; L. Ricci et al. 2015; M. A. MacGregor et al. 2016). Densities of 2.7 and 0.92 g cm⁻³ are assumed for silicate and ice grains, respectively, as expected for submicron grains in KBOs (C. M. Lisse et al. 1998). The evolution of the size, hence β , due to UV photospattering or solar-wind-induced sputtering is followed by simultaneously integrating it with Equation (1).

Equation (1), with the addition of gravitational forces from Jupiter, Saturn, Uranus, and Neptune, is integrated using a fourth/fifth-order adaptive stepsize Runge–Kutta–Fehlberg method (E. Fehlberg 1969; W. H. Press et al. 2002), which

accurately resolves close encounters with the planets. All KBOs are included in the model as source objects. To achieve similar statistics for both populations, a total of 10,000 silicate grains and 500,000 ice grains were simulated for each KBO database/model. Grains are only removed from the simulation when their orbital energy becomes greater than zero, indicating an unbound orbit, or their mass falls below the SDC detection threshold. A slice of the 3D equilibrium density distribution, extending ± 0.5 au above and below the ecliptic plane, is used to compare directly with SDC measurements.

5. Results

Figure 3 shows the equilibrium number density profiles of silicate and ice grains near the ecliptic, fitted to SDC data using χ^2 minimization (W. H. Press et al. 2002) varying only the silicate and ice production rates, keeping all other simulation variables constant. Contrary to expectations, the debiased KBO models CFEPS and OSSOS, which include many more distant objects, do not exhibit a more distant silicate number density peak as compared to the observational SBDB database. Instead, silicate number densities between 40 and 60 au are slightly lower in the debiased models because dust from the distant, high-inclination KBOs do not contribute to the equilibrium number density profile near the ecliptic as much as closer, low-inclination KBOs would. Despite these variations in the silicate equilibrium distribution, the silicate mass production rate remains generally consistent across all KBO models.

The ice number density peak is more distant than the silicate peak. Most ice grains initially migrate outward due to radiation pressure and erosion and have a negligible contribution within Neptune's orbit. Due to their shorter lifetimes and greater heliocentric distances, ice grains have lower number densities than silicate grains at the same production rates, necessitating a higher ice production rate to fit SDC data. This finding is consistent with the ice content of KBOs (M. E. Brown 2012; M. E. Brown & W. C. Fraser 2023) and laboratory impact crater experiments, which show that the ejected mass yield increases by over 1 order of magnitude, going from a pure silicate to a pure ice surface (M. A. Lange & T. J. Ahrens 1987; D. Koschny & E. Grün 2001). This tendency of enhanced yield with increasing ice content was also observed by the Galileo mission in the dust exospheres engulfing the large icy moons of Jupiter (A. V. Krivov et al. 2003).

Table 1 lists our estimates for silicate and ice production rates in the KB. Previous estimates of the KB silicate mass production rate matching early SDC data were in the range of 8.4×10^5 – 9.4×10^5 (D. Han et al. 2011) and 6×10^6 – 1×10^7 g s⁻¹ (A. R. Poppe et al. 2019). These models were constrained by available SDC data out to only 20 and 40 au, respectively. Consequently, these production rates were not informed by the measured dust densities beyond 40 au.

Theoretical estimates for the mass production rate in the KB are 8.6×10^4 – 2.9×10^7 g s⁻¹ from mutual collisions (S. A. Stern 1996) and 3.7×10^5 – 3.1×10^7 g s⁻¹ from interstellar dust bombardment (S. Yamamoto & T. Mukai 1998). Our model results are consistent with the upper ranges of these estimates. The wide range of theoretical estimates should be revisited based on our more complete recent understanding of the KB (R. Malhotra 2019) and the interstellar dust flux (H. Krüger & E. Grün 2009).

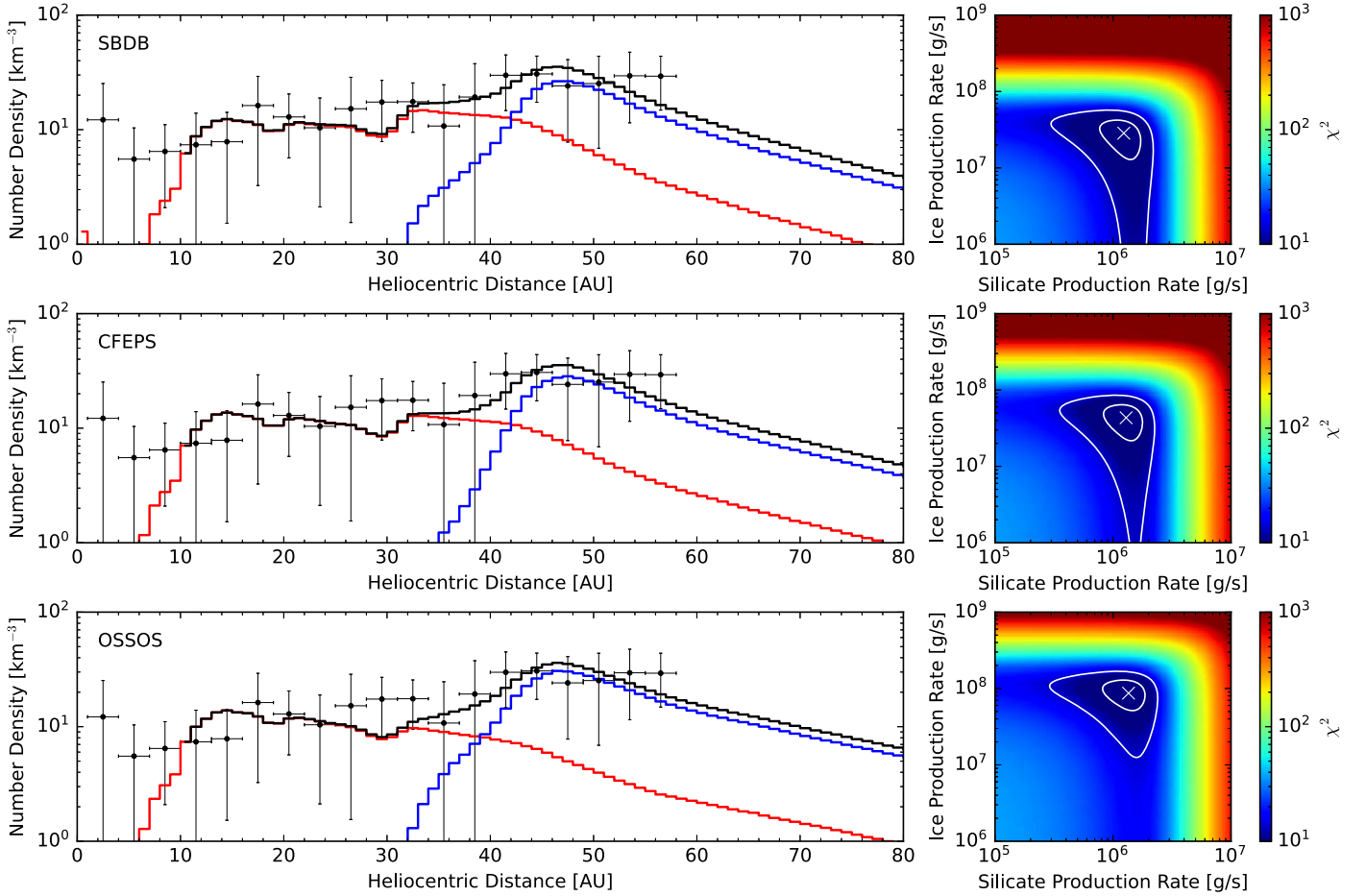


Figure 3. Left: equilibrium number density profiles of silicate and ice grains near the ecliptic and above the SDC mass threshold as a function of heliocentric distance using the SBDB (top), CFEPS (middle), and OSSOS (bottom) KBO databases/models. The combined modeled number density (black) of silicate (red) and ice (blue) grains is fitted to SDC data with 1σ error bars (black) for heliocentric distances greater than 10 au. Right: corresponding χ^2 maps of silicate and ice mass production rates for each KBO database/model with best-fit production rates (white crosses). Regions of confidence corresponding to a significance level of $\alpha = 0.68$ and $\alpha = 0.99$, or 1σ and 3σ , respectively, are encircled in white lines. The 1σ production rate ranges can be found in Table 1.

Table 1

Mass Production Rates of 0.1–10 μm Silicate and Ice Grains for Various KBO Databases/Models Fitted to SDC Data in the 1σ Significance Level

KBO Database/Model	Silicate Production Rate (g s^{-1})	Ice Production Rate (g s^{-1})	Ice to Silicate Production Ratio
SBDB	7.7×10^5 – 1.7×10^6	1.3×10^7 – 4.2×10^7	~ 20
CFEPS	8.3×10^5 – 1.8×10^6	2.2×10^7 – 6.4×10^7	~ 30
OSSOS	8.1×10^5 – 1.9×10^6	5.1×10^7 – 1.3×10^8	~ 70

6. Discussion

The model discussed so far focused on pure silicate and water–ice grains. In reality, grains are likely composed of a mixture of rocky, carbonaceous, and volatile matter (J. A. Burns et al. 1979; A. Grigorieva et al. 2007; M. E. Brown & W. C. Fraser 2023), with dynamical evolution that might not be bracketed by the assumed single-composition grains modeled here.

Thus, we briefly explore two scenarios of refractory/volatile mixtures: well-mixed and differentiated grains. For well-mixed grains, we approximate the radiation pressure coefficient as a surface-fraction-weighted average. Since weakly bound grains also lose rocky material with eroding ice, we keep the ice mass fraction fixed and approximate the erosion rate also as a surface-fraction-weighted average. This simplification keeps the volatile–refractory ratio constant and avoids the complexity

of developing differentiated layers within a dust grain. For differentiated grains with a rocky core and ice mantle, we use the radiation pressure coefficient and erosion rate for pure ice until the mantle erodes, at which point we switch to those of pure silicate.

Figure 4 shows the equilibrium distributions of grains for both cases. The equilibrium distribution for well-mixed grains resembles that of pure ice but with higher number densities due to the slower erosion and therefore longer lifetimes. For differentiated grains, the equilibrium distribution resembles that of pure silicate but with lower number densities because the ice mantle rapidly erodes and the grain eventually behaves like pure silicate, but grains can drop below the SDC mass threshold in this process. The preliminary results indicate that even a low ice content can have a large impact on equilibrium distributions, suggesting that the ice production rate may not

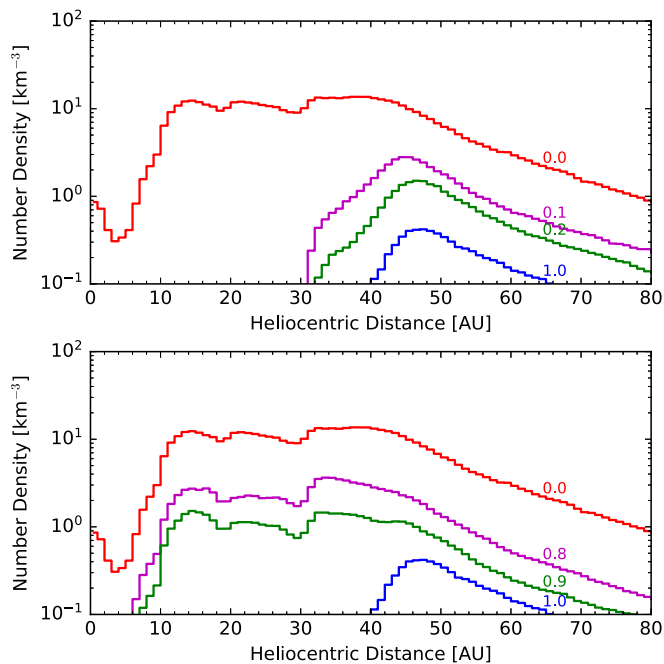


Figure 4. Equilibrium number density profiles of well-mixed (top) and differentiated (bottom) grains near the ecliptic and above the SDC mass threshold as a function of heliocentric distance using the SBDB KBO database. Each histogram is labeled with its corresponding ice mass fraction. The same number of grains is produced for each case, matching the best-fit silicate production rate for the SBDB KBO database in Table 1.

need to be as high to fit SDC data. These rough models are intended simply to motivate future research that captures more realistic grain compositions and behaviors.

7. Conclusion

We have estimated the equilibrium distributions and mass production rates of silicate and ice grains in the outer solar system using various KBO databases/models as source objects. This work suggests that the equilibrium dust distributions are relatively independent of the three source object distributions we used and are more dependent on the assumed composition of the grains. Hence, without measuring grain composition, SDC measurements to date do not fully constrain the extent of the KB.

For the case in which pure silicate and pure ice grains are produced, we estimate that the mass production rate of 0.1–10 μm ice grains is 20–70 times higher than for silicate grains, consistent with the ice content of KBOs (M. E. Brown 2012; M. E. Brown & W. C. Fraser 2023) and the high yield from impacts on these surfaces (M. A. Lange & T. J. Ahrens 1987; D. Koschny & E. Grün 2001; A. V. Krivov et al. 2003). These estimates should be refined for the more realistic cases of mixed-composition grains.

Significant deviation from the predicted decline of dust densities in future SDC measurements would prompt us to revisit the assumptions used in this model. A continued increase in measured dust densities may suggest an undiscovered, unexpectedly massive population of distant source objects, while a more rapid decrease in measured dust densities may suggest refractory dominant or differentiated grain compositions that, dynamically, look like silicate grains.

The suggestion of distant icy grains has implications for our understanding of dust disks and may impact the interpretation of observed extrasolar dust disks, as similar processes are expected

to occur in other solar systems (K. M. Pontoppidan et al. 2005; H. Terada et al. 2007; C. H. Chen et al. 2008; M. Honda et al. 2009). Advances in detecting both the spatial distributions and compositions of extrasolar dust disks will enhance our understanding of these processes (A. M. Hughes et al. 2018; M. Kim et al. 2024). The distinct dynamics of the inwardly migrating refractory and the outwardly migrating volatile grains result in composition-differentiated spatial distributions that, when resolved, may help constrain the spatial distribution of the corresponding extrasolar source objects.

Continued SDC measurements at greater heliocentric distances will further constrain our models of the production, transport, and destruction of dust in the outer solar system.

ORCID iDs

Thomas Corbett <https://orcid.org/0009-0004-3314-2870>
 Alex Doner <https://orcid.org/0000-0001-7065-3224>
 Mihály Horányi <https://orcid.org/0000-0002-5920-9226>
 Pontus Brandt <https://orcid.org/0000-0002-4644-0306>
 Will Grundy <https://orcid.org/0000-0002-8296-6540>
 Carey M. Lisse <https://orcid.org/0000-0002-9548-1526>
 Joel Parker <https://orcid.org/0000-0002-3672-0603>
 Lowell Peltier <https://orcid.org/0000-0002-9179-8323>
 Andrew R. Poppe <https://orcid.org/0000-0001-8137-8176>
 Kelsi N. Singer <https://orcid.org/0000-0003-3045-8445>
 S. Alan Stern <https://orcid.org/0000-0001-5018-7537>
 Anne J. Verbiscer <https://orcid.org/0000-0002-3323-9304>

References

- Bagenal, F., Horányi, M., McComas, D. J., et al. 2016, *Sci*, **351**, aad9045
 Bannister, M. T., Gladman, B. J., Kavelaars, J. J., et al. 2018, *ApJS*, **236**, 18
 Bannister, M. T., Kavelaars, J. J., Petit, J.-M., et al. 2016, *AJ*, **152**, 70
 Belousov, D. V., & Pavlov, A. K. 2024, *Icar*, **415**, 116066
 Bernardoni, E., Horányi, M., Doner, A., et al. 2022, *PSJ*, **3**, 69
 Brown, M. E. 2012, *AREPS*, **40**, 467
 Brown, M. E., & Fraser, W. C. 2023, *PSJ*, **4**, 130
 Burns, J. A., Lamy, P. L., & Soter, S. 1979, *Icar*, **40**, 1
 Carlson, R. W. 1980, *Natur*, **283**, 461
 Chen, C. H., Fitzgerald, M. P., & Smith, P. S. 2008, *ApJ*, **689**, 539
 Danby, J. M. A. 1992, *Fundamentals of Celestial Mechanics* (Washington, DC: Willmann-Bell)
 Dohnanyi, J. S. 1969, *JGR*, **74**, 2531
 Doner, A., Horányi, M., Bagenal, F., et al. 2024, *ApJL*, **961**, L38
 Fehlbeg, E. 1969, *Low-order Classical Runge–Kutta Formulas with Stepsize Control and their Application to Some Heat Transfer Problems*, Technical Report NASA-TR-R-315
 Fountain, G., Weaver, H., Reuter, D., et al. 2023, *The New Horizons Instrument Suite*, Technical Digest 37-1, Johns Hopkins APL
 Fraser, W. C., Porter, S. B., Peltier, L., et al. 2024, *PSJ*, **5**, 227
 Gladman, B. & CFEPS Team 2010, *AAS/DPS Meeting Abstracts*, **42**, 40.11
 Grigorieva, A., Thébault, P., Artymowicz, P., & Brandeker, A. 2007, *A&A*, **475**, 755
 Han, D., Poppe, A. R., Piquette, M., Grün, E., & Horányi, M. 2011, *GeoRL*, **38**, 24102
 Harrison, H., & Schoen, R. I. 1967, *Sci*, **157**, 1175
 Honda, M., Inoue, A. K., Fukagawa, M., et al. 2009, *ApJL*, **690**, L110
 Horányi, M., Hoxie, V., James, D., et al. 2008, *SSRv*, **140**, 387
 Hughes, A. M., Duchêne, G., & Matthews, B. C. 2018, *ARA&A*, **56**, 541
 James, D., Hoxie, V., & Horányi, M. 2010, *RSci*, **81**, 034501
 Kavelaars, J. J., Jones, R. L., Gladman, B. J., et al. 2009, *AJ*, **137**, 4917
 Kim, M., Kennedy, G. M., & Roccatagliata, V. 2024, *MNRAS*, **533**, 2801
 Koschny, D., & Grün, E. 2001, *Icar*, **154**, 391
 Krivov, A. V., Sremčević, M., Spahn, F., Dikarev, V. V., & Kholshchikov, K. V. 2003, *P&SS*, **51**, 251
 Krüger, H., & Grün, E. 2009, *SSRv*, **143**, 347
 Landgraf, M., Liou, J.-C., Zook, H. A., & Grün, E. 2002, *AJ*, **123**, 2857
 Lange, M. A., & Ahrens, T. J. 1987, *Icar*, **69**, 506
 Lawler, S. M., Kavelaars, J. J., Alexandersen, M., et al. 2018, *FRASS*, **5**, 14

- Liou, J.-C., Zook, H. A., & Jackson, A. A. 1999, *Icar*, **141**, 13
- Lisse, C. M., A'Hearn, M. F., Hauser, M. G., et al. 1998, *ApJ*, **496**, 971
- Lisse, C. M., Young, L. A., Cruikshank, D. P., et al. 2021, *Icar*, **356**, 114072
- MacGregor, M. A., Lawler, S. M., Wilner, D. J., et al. 2016, *ApJ*, **828**, 113
- Malhotra, R. 2019, *GSL*, **6**, 12
- Mukai, T., Blum, J., Nakamura, A. M., Johnson, R. E., & Havnes, O. 2001, in *Interplanetary Dust*, ed. M. A. Barucci et al. (Berlin: Springer), 445
- Patashnick, H., & Rupperecht, G. 1977, *Icar*, **30**, 402
- Petit, J. M., Kavelaars, J. J., Gladman, B. J., et al. 2011, *AJ*, **142**, 131
- Piquette, M., James, D., & Horányi, M. 2020, *RSci*, **91**, 023307
- Piquette, M., Poppe, A. R., Bernardoni, E., et al. 2019, *Icar*, **321**, 116
- Pontoppidan, K. M., Dullemond, C. P., van Dishoeck, E. F., et al. 2005, *ApJ*, **622**, 463
- Poppe, A., James, D., Jacobsmeyer, B., & Horányi, M. 2010, *GeoRL*, **37**, 11101
- Poppe, A. R. 2016, *Icar*, **264**, 369
- Poppe, A. R., Lisse, C. M., Piquette, M., et al. 2019, *ApJL*, **881**, L12
- Press, W. H., Teukolsky, S. A., Vetterling, W. T., & Flannery, B. P. 2002, *Numerical Recipes in C++ : The Art of Scientific Computing* (Cambridge: Cambridge Univ. Press)
- Ricci, L., Carpenter, J. M., Fu, B., et al. 2015, *ApJ*, **798**, 124
- Stern, S. A. 1996, *A&A*, **310**, 999
- Szalay, J. R., Piquette, M., & Horányi, M. 2013, *EP&S*, **65**, 1145
- Terada, H., Tokunaga, A. T., Kobayashi, N., et al. 2007, *ApJ*, **667**, 303
- Wyatt, S. P., & Whipple, F. L. 1950, *ApJ*, **111**, 134
- Yamamoto, S., & Mukai, T. 1998, *A&A*, **329**, 785